Spicule-like structures observed in 3D realistic MHD simulations

Juan Martínez-Sykora¹

j.m.sykora@astro.uio.no

Viggo Hansteen¹

viggo.hansteen@astro.uio.no

Bart De Pontieu²

bdp@lmsal.com

and

Mats Carlsson¹

m.p.o.carlsson@astro.uio.no

¹ Institute of Theoretical Astrophysics, University of Oslo, P.O. Box 1029 Blindern, N-0315 Oslo, Norway

² Lockheed Martin Solar & Astrophysics Lab, Palo Alto, CA94304, USA

ABSTRACT

We analyze features that resemble type I spicules in two different 3D numerical simulations in which we include horizontal magnetic flux emergence in a computational domain spanning the upper layers of the convection zone to the lower corona. The two simulations differ mainly in the preexisting ambient magnetic field strength and in the properties of the inserted flux tube. We use the Oslo Staggered Code (OSC) to solve the full MHD equations with non-grey and non-LTE radiative transfer and thermal conduction along the magnetic field lines. We find a multitude of features that show a spatiotemporal evolution that is similar to that observed in type I spicules, which are characterized by parabolic height vs. time profiles, and are dominated by rapid upward motion at speeds of 10-30 km s⁻¹, followed by downward motion at similar velocities. We measured the parameters of the parabolic profile of the spicules and find similar correlations between the parameters as those found in observations. The values for height (or length) and duration of the spicules found in the simulations are

more limited in range than those in the observations. The spicules found in the simulation with higher preexisting ambient field have shorter length and smaller velocities. From the simulations, it appears that these kinds of spicules can, in principle, be driven by a variety of mechanisms that include p-modes, collapsing granules, magnetic energy release in the photosphere and lower chromosphere and convective buffeting of flux concentrations.

Subject headings: Magnetohydrodynamics MHD —Methods: numerical — Radiative transfer — Sun: atmosphere — Sun: magnetic field

1. Introduction

The chromosphere is filled with jet-like features, such as dynamic fibrils (active regions on the disk), mottles (quiet Sun on the disk) and spicules of different types (at the limb). Recently, significant improvements in the spatiotemporal resolution of observations with Hinode (Tsuneta et al. 2008) and with the Swedish 1-m Solar Telescope (SST) (Scharmer et al. 2008) to 100 km and a few seconds cadence have revealed a complex mix of highly dynamic structuring on small spatial scales (De Pontieu et al. 2007b; Hansteen et al. 2006; De Pontieu et al. 2007a). There has been a long-standing discussion on whether and how these different structures are related (Beckers 1968).

At the limb, several different types of thin, elongated features, or spicules, are observed in H α and other chromospheric lines. They are characterized by dynamics on different timescales, with so-called type I spicules occurring on timescales of order 3-10 minutes, and type II spicules having lifetimes that are typically less than 100 seconds. The first type develops speeds of 10-30 km s⁻¹, reaches heights of 2-9 Mm (Beckers 1968) and typically involves upward motion followed by downward motion. The second type of spicules are more violent with speeds of order 50-100 km s⁻¹, similar heights, and usually only upward motion (De Pontieu et al. 2007b). In this paper we focus on a subset of the more slowly developing, first type of spicules.

Recent studies have suggested a close relationship between these type I spicules and dynamic fibrils in active regions, and some quiet Sun mottles (Hansteen et al. 2006; De Pontieu et al. 2007b; Rouppe van der Voort et al. 2007). Dynamic fibrils dominate the chromospheric dynamics above plage regions in active regions, when observed at disk center. They are characterized by up- and downward motion that follows a parabolic path as a function of time. Typically, the deceleration in this parabolic path is different from solar gravitational acceleration. Similar features, so called dark mottles, are seen in and around small flux concentrations

of the quiet Sun magnetic network. The similarity in dynamic behavior of mottles, dynamic fibrils and some type I spicules with up- and downward parabolic motion, and significant correlations between parabolic parameters such as deceleration and maximum velocity strongly suggest that these features are driven by the same mechanism. Hansteen et al. (2006) and De Pontieu et al. (2007a) found jet-like features with similar properties in self-consistently driven 2D-MHD simulations. The jet-like features in these simulations were found to be caused by shock-waves driven by leakage of convective motions and oscillations from the photosphere into the chromosphere along magnetic field concentrations. This is the mechanism originally suggested by De Pontieu et al. (2004) to explain the quasi-periodicities observed in dynamic fibrils that permeate the upper transition region of coronal loops (De Pontieu et al. 2003). Heggland et al. (2007) used a wide variety of 1D simulations to show that a mechanism in which shock waves drive these jets can naturally explain the correlations between parabolic parameters that was found in the observations and 2D simulations.

In this paper we take the logical next step and analyze similar jet-like features that we find in 3D-MHD simulations. These simulations are quasi-realistic and include non-grey and non-LTE radiative transfer with scattering and thermal conduction along the magnetic field lines. The simulations include the upper layers of the convection zone up to the lower corona. The organization of the paper is as follows: \S 2 briefly describes the numerical methods, initial conditions and boundaries employed in the numerical code. In \S 3.1, we describe the correlation between the properties of the 150 spicule-like features that we found in the simulations. While all of these spicule-like features seem to be driven by magnetoacoustic shocks, we find that a variety of events can produce such waves (\S 3.2). The physics and dynamics of the spicules and the detailed evolution of the formation mechanism are described in \S 3.3. We finish this paper with a discussion in \S 4.

2. Equations and numerical method

The numerical model uses the Oslo Stagger Code (OSC) which solves the MHD equations in a domain that stretches from the upper convection layer up to the corona. The MHD equations are solved using an extended version of the numerical code described in Dorch & Nordlund (1998); Mackay & Galsgaard (2001) and in more detail by Nordlund & Galsgaard at http://www.astro.ku.dk/~kg and Martínez-Sykora et al. (2008, 2009) (we will refer to the latter two papers as Paper I and Paper II, respectively). The code functions as follows. A sixth order accurate method involving the three nearest neighbor points on each side is used for determining the spatial partial derivatives combined with a fifth order interpolation scheme. The equations are stepped forward in time using the explicit third order

predictor-corrector procedure by Hyman et al. (1979), modified for variable time steps. In order to suppress numerical noise, high-order artificial diffusion is added both in the forms of a viscosity and magnetic diffusivity (Paper II).

The radiative flux divergence from the photosphere and lower chromosphere is obtained by angle and wavelength integration of the transport equation assuming isotropic opacities and emissivities. The transport equation assumes opacities in LTE using the solution based on four group mean opacities (Nordlund 1982). The transfer equation is formulated for these bins and a group mean source function is calculated for each bin. These source functions contain an approximate coherent scattering term and an exact contribution from thermal emissivity. The resulting 3D scattering problems are solved by iteration based on one-ray approximation in the angle integral for the mean intensity as developed by Skartlien (2000).

In the mid and upper chromosphere OSC includes non-LTE radiative losses from hydrogen continua, hydrogen lines and lines from singly ionized calcium. These losses are calculated from the local net collisional excitation rate multiplied by an escape probability that is based on a 1D dynamical chromospheric model in which the radiative losses are computed in detail (Carlsson & Stein 1992, 1995, 1997, 2002). In addition to these radiative losses in the upper atmosphere we have added an *ad hoc* heating term to prevent the atmosphere from cooling much below 2000 K in the upper chromosphere.

For the upper chromosphere and corona we assume optically thin radiative losses. The optically thin radiative loss function is based on the coronal approximation and atomic data collected in the HAO spectral diagnostics package (Judge & Meisner 1994) for the elements hydrogen, helium, carbon, oxygen, neon and iron.

The code includes thermal conduction along the magnetic field. The conduction equations are discretized using the Crank-Nicholson method and the resulting operator is solved by operator splitting. We solve the implicit part of the conduction problem using a multigrid solver. There is also a more detailed description of the radiative losses and thermal conduction in Paper I.

2.1. Initial and boundary conditions

The numerical simulation described here is the same as in Paper II which has a grid size of $256 \times 128 \times 160$ points spanning $16 \times 8 \times 16$ Mm³. The horizontal resolution is uniform at 65 km while the vertical grid is non-uniform; thus ensuring that the vertical resolution is good enough to resolve the photosphere and the transition region with a grid spacing of 32.5 km, while becoming larger at coronal heights. At this resolution the simulations have

been run for roughly 1.5 hours of solar time.

We have seeded the initial model with a magnetic field in which sufficient stresses can be built up to maintain coronal temperatures in the upper part of the computational domain, as previously shown to be feasible by Gudiksen & Nordlund (2004). We introduce a magnetic flux tube into the lower boundary parallel to the y-axis and centered roughly at 8 Mm (see right panel of Fig 2). This is described in detail in Paper I, \S 3.2. The magnetic flux tube structure is horizontal and axisymmetric:

$$\mathbf{B}_{l} = B_{o} \exp\left(-\frac{r^{2}}{R^{2}}\right) \mathbf{e}_{z}, \tag{1}$$

$$\mathbf{B}_t = B_l \, r \, q \, \mathbf{e}_{\phi}, \tag{2}$$

where $r = \sqrt{(x - x_o)^2 + (z - z_o)^2}$ is the radial distance to the center of the tube and R is the radius of the tube. \mathbf{B}_l and \mathbf{B}_t are the longitudinal and transversal magnetic fields in cylindrical coordinates, respectively. Note that the longitudinal field has a gaussian profile. The parameter q is used by Linton et al. (1996) and Fan et al. (1998) to define the twist of the magnetic field. Following Cheung et al. (2006), we define a non-dimensional twist parameter ($\lambda \equiv q R$).

We have run two different simulations. The parameters of the tube, R, B_o and λ , for each simulation are given in table 1. The emerging flux tube in simulation A2 has $B_0 = 4500$ G at the bottom boundary, with twist $\lambda = 0.6$. The emerging flux tube in simulation B1 has $B_0 = 1100$ G and no twist.

As the flux tube enters the computational box, the height of the center of the tube (z_o) changes in time. At each time step, the speed of the flux tube, (dz_o/dt) , is set to the average of the velocity of plasma inflow at the boundary in the region where the magnetic flux tube is located.

We have analyzed simulations A2 and B1 from Paper II searching for jet-like features. In both simulations, the initial coronal loops are generally aligned along the x-axis, stretching from magnetic field concentrations centered roughly at x=7 Mm and x=13 Mm (see the field line distribution in Fig. 1 in Paper II and right panel of Fig. 2 of this paper). Simulation A2 has an average unsigned field strength in the photosphere of 16 G, whereas simulation B1 has a field strength of 160 G. A summary of the simulation properties is shown in table 1.

3. Results

The simulations produce a variety of different jets which show similarities to both type I and type II spicules. These jets are formed by the natural evolution of the 3D model, *i.e.*, without imposing any additional conditions. Here, we extend the work done by De Pontieu et al. (2007a) and Heggland et al. (2007) to 3D and study the effects of flux emergence by analyzing two different models, with differing values of the pre-existing magnetic field and the magnetic flux tube. We will concentrate our attention on the jets that show dynamical behaviour similar to that of type I spicules. Henceforth we call the jets observed in our simulations spicules.

3.1. Properties

We found a total of 168 candidate type I spicules in the two different simulations, A2 and B1. To find these features, we use 3D images of the transition region and select only jet-like features that reach a height larger than 2000 km above the photosphere. Once identified, we plot for each spicule, the temperature as a function of time and height (see top panels of Fig. 6). We then fit the trajectory of the transition region (at $T = 10^5$ K) with a parabola. We reject the jets that do not have a parabolic evolution, or have lengths that are less than 500 km. We are left with 150 spicules which we study in more detail below.

Once the motion of the transition region in these spicules has been fit with a parabolic trajectory, we measure the following parameters: maximum length, duration, maximum velocity, deceleration and the angle of the magnetic field with respect to the vertical. Given that most spicules are close to vertical and quite wide, we take into account their non-verticality by correcting these parameters with the cosine of the magnetic field angle with respect to the vertical. Figure 1 shows scatterplots illustrating the relation between some of these parameters; for instance, deceleration vs. duration, deceleration vs. maximum velocity of the spicule etc.

Comparison of Fig. 1 with Figs. 12 and 13 from De Pontieu et al. (2007a) shows remarkable similarities of the correlations between the various parameters of the jets in our simulations and those found for dynamic fibrils from observations. Similar to the dynamic fibrils, we find that the spicules in the simulations with longer duration have smaller deceleration. In addition, spicules that are longer have higher deceleration, and the higher the deceleration, the higher the maximum velocity is. Spicules with longer duration are typically longer, and the longer spicules have higher maximum velocity. There does not appear to be much correlation between duration and maximum velocity. All of these relations fit well

with those observed in dynamic fibrils, quiet Sun mottles and type I spicules. Moreover, the range of values for deceleration and maximum velocities are similar for observations and simulations.

There are also differences between the simulations and observations, particularly with respect to the range of values that are found for duration and length. These are found to have a smaller range in the simulations than in the observations. Most durations are around 3 minutes, instead of the wide range of durations between 2 and 8 minutes found in the observations. All of the spicules that form in the models are broader than in the observations, most likely because the numerical resolution is relatively low. The simulated spicules are also shorter in length than in the observations. These discrepancies are discussed in § 4.

The role of the magnetic configuration and/or field strength is illustrated by the fact that the values we find in the simulations seem more in line with those found in region 2 of De Pontieu et al. (2007a), i.e., a denser plage region, which showed shorter fibrils with durations of order 180 s. In addition, we find that the maximum velocity, deceleration, and maximum length are all smaller for the spicules we find in simulation B1 (red symbols in Fig. 1). We find that the number of spicules per unit time is higher with higher ambient magnetic field (i.e., simulation B1). There seems to be a trend towards a slightly different correlation between duration and maximum length, and duration and deceleration for the two different runs. We generally do not see any significant differences in these correlations for the two different periods, during and after flux emerges through the photosphere, in simulation A2 (black and blue in Fig. 1, respectively).

While all of these spicules are driven by magnetoacoustic shocks, the waves that develop into these shocks are caused by a variety of drivers. We describe in detail in § 3.2 the different drivers we have identified from the simulations: collapsing granules (plus signs in Fig. 1), magnetic energy release in the photosphere (rhombi in Fig. 1) and magnetic energy release in lower chromosphere (triangles in Fig. 1). There seem to be some differences in correlations for spicules caused by different drivers. The spicules driven by chromospheric magnetic energy release (triangles) are located in the upper part of the scatter plot showing the correlation between deceleration and maximum velocity (middle left panel of Fig. 1) and of the scatterplot showing the correlation between maximum velocity and maximum length (bottom right panel of Fig. 1). Other than these differences, the various driving mechanisms do not seem to lead to any other differences in the correlation plots.

When considering the location of the occurrence of spicules we find that all the spicules we have identified are concentrated at the foot points of coronal loops as seen in Figure 2. In the right panel of Figure 2 we draw a set of field lines computed by integrating from

randomly chosen points in a horizontal plane high in the corona. These field lines all tend to have their foot points along two lines oriented roughly in the y-direction. In addition, the field lines are roughly vertical as they pierce the photosphere. It is along these field lines that our spicules propagate. During the evolution of the flux emergence in simulation A2 the left foopoints of the coronal loops move leftward. This is clearly reflected in the spicules distribution (Fig. 2): spicules after flux emergence, shown in blue, are further left than the spicules that occur before and during (black).

3.2. Driving mechanism

Analysis of our simulations tells us that the spicule-like features are produced by magnetoacoustic shocks which form when waves that are generated in the photosphere or lower chromosphere propagate through to the chromosphere and shock because of the rapid drop in density with height. The magnetoacoustic shock drives plasma upwards, leading to a rapid upward motion of the transition region, followed by a downward motion after passage of the shock (see § 3.3.1 for details). This behavior is identical to the scenario outlined by Hansteen et al. (2006). The time delay between the generation of the wave and the formation of the spicule depends strongly on the length of the trajectory. For instance, a wave generated in the photosphere takes roughly 3 minutes to reach the transition region, whereas it only takes roughly 1.5 minutes from the lower chromosphere. It seems that two conditions must be satisfied in order to produce spicule-like features in our simulations: 1) The waves require strong magnetic flux concentrations to guide them upward; 2) The field must extend into the corona which in our models occurs only for field lines with angles with respect to the vertical between $0-30^{\circ}$. Figure 3 illustrates the range of angles from the vertical in all spicules we analyzed. We find that the angles do not depend on the magnetic field strength and/or flux emergence properties. The mostly vertical field we measure might be caused by a selection effect since the selection criterion we use to identify spicules requires a minimum height of 2000 km. Given the short lengths of the spicules produced, this criterion favors more vertically oriented spicules, since these are the only field lines that reach the corona (see also $\S 4$).

In order to determine the driver, we analyze one or more magnetic field lines that follow the spicule's long axis, and we identify the shock front. We trace the shock front back until the time when the shock is formed. Once we localize the place and instant of shock formation, we analyze the surroundings of that region and try to find which kind of process perturbs the region enough to produce a wave. In most cases this is quite difficult because of the complex mix of events that occur in our 3D simulations. In many cases we find that the wave could be excited by several different physical processes, whereas in other cases we are unable to identify a dominant cause; we will refer to these unidentified drivers as "other mechanisms". Generally, we find that the most frequent processes that cause these waves are: p-mode oscillations, collapsing granules, breaking granules, flux emergence through the photosphere, magnetic energy release in the photosphere or in the lower chromosphere. This is by no means a complete list, because, as just mentioned, it is often difficult to identify the driver.

The easiest drivers to identify are collapsing granules, magnetic energy release in the photosphere, and magnetic energy release in the chromosphere. However, in most cases, it is difficult to have 100% confidence in the identification. The number of spicules caused by the different drivers is different for both simulations: for simulation A2, the percentage of spicules caused by collapsing granules, magnetic energy release in the photosphere, magnetic energy release in the chromosphere and other mechanisms is respectively, 26%, 29%, 19% and 26%. For simulation B1 with higher ambient field, these numbers are 42%, 26%, 6% and 26%. Magnetic energy release in the chromosphere thus contributes significantly less to the formation of spicules when the ambient magnetic field is stronger (perhaps because most magnetic energy release occurs lower down, since emerging flux encounters significant flux at lower heights). In both simulations a significant amount of flux emerges. This contributes in different ways to the excitation of the shock waves that drive the spicules. There is a peak in the number of spicules driven by collapsing granules when the flux is first entering the photosphere from below. Afterwards, spicules driven by magnetic energy release in the photosphere dominates, since there appears to be an interaction between the rising flux tube and the ambient field. Generally, the spicules driven by collapsing granules seem more prevalent in the weak ambient field simulation (A2) where the flux tube perturbs the granulation pattern more profoundly.

A collapsing granule produces a perturbation or wave that affects temperature and pressure and propagates in all directions (see § 3.3.1) (Skartlien et al. 2000). It can perturb one or more flux concentrations and produces spicules when the disturbance propagates along flux concentrations. In figure 4 we show an example where a spicule is formed because of a wave triggered by a collapsing granule that is surrounded by two different flux concentrations in the photosphere (right panel). It is unclear which of the two flux concentrations is dominant in the spicule formation because the numerical resolution is too low. We see that the field lines along which the spicule forms are quite vertical and go into the corona. The presence of a strong flux concentration and field lines that enter into the corona, generally allow for easier propagation of the perturbations from the photosphere into the chromosphere and the corona, thus facilitating the formation of spicules in our simulations.

The deposition of thermal energy as a result of magnetic energy dissipation can produce a perturbation or wave that can steepen into a shock when propagating into the chromosphere along a large flux concentration (see § 3.3.1). We tentatively call these events "magnetic energy release". They usually are not as concentrated in space and time and thus as explosive as typical reconnection events observed in the solar atmosphere (e.g., explosive events in which the dominant component of the field shows opposite polarity). In fact, in many cases we do not find opposite polarity field lines at the location of the driver. We often find more gentle dissipation of currents to be the driving mechanism. The magnetic energy release sources that we manage to identify are concentrated in the upper photosphere and lower chromosphere. In what follows we call magnetic dissipation related events "photospheric magnetic energy release" if the event occurs at heights of 0 < z < 500 km, and "chromospheric magnetic energy release" for 500 < z < 1000 km.

To study where current dissipation or magnetic energy release takes place in our simulations, we use the following parameter:

$$R_d = \frac{|\mathbf{J}|}{\sqrt{P}} \tag{3}$$

where P and \mathbf{J} are the gas pressure and the current density, respectively. This parameter shows the discontinuity of the magnetic field since it is proportional to the magnetic field strength (and inversely proportional to the length scale over which it changes). It is a good proxy to identify where the current is important and the location of current sheets. Usually, the discontinuity of the magnetic field is shown with $|\mathbf{J}|/|\mathbf{B}|$. However, several regions in our models have field that is weak or almost zero, e.g., in the upper part of the corona or in the convection zone, which makes it difficult to evaluate $|\mathbf{J}|/|\mathbf{B}|$ numerically. This is why we normalized with the square root of the pressure instead of using the magnetic field strength.

Figure 5 shows two examples in which magnetic energy is released and spicules are formed as a result. In the left image, three different spicules occur around the same time. They can all be traced back to a magnetic event that takes place in the photosphere, in a single flux concentration. The right panel shows the formation of a spicule as a result of magnetic energy release in the lower chromosphere (green-blue color scale, where R_d is high). All field lines that are involved in the spicules are associated with locations of high R_d , i.e., the lines are associated with magnetic energy release events. In the example on the left, we see that the same magnetic energy release process (in the photosphere) can trigger more than one spicule at the same time. When the magnetic energy release occurs higher up (right image), it seems more difficult to produce more than one spicule from the same

event. This may be because the path from the source to the transition region is shorter and does not allow differential propagation of the wave that forms the spicule(s).

We observed of the order of 20 examples where one specific excitation event seems to produce several spicules. The source (collapsing granule, p-modes, and magnetic energy release in the photosphere) is able to perturb several magnetic flux concentrations (or even the same flux concentration) and produces several spicules as a result. These spicules are excited by the same driver and occur close in time and space. This phenomenon is similar to what has been reported in observations of dynamic fibrils by De Pontieu et al. (2007a).

Returning to the location of spicule generation shown in figure 2, we note that during flux emergence through the photosphere it is more common to find spicules driven by collapsing granules at the footpoints of the loop situated within x = [5-8] Mm, where the emerging flux is located. This is presumably because the granular dynamics are heavily perturbed by the flux emergence. At later times (locations plotted in blue) flux emergence does not perturb the granulation pattern as much, and the occurrence and distribution of the spicule types is similar in both of the footpoint bands located at x = [5-8] Mm and at x = [13-15] Mm in the photosphere. In simulation B1, the strength of the emerging magnetic flux is lower and the ambient magnetic field is stronger than in simulation A2. Thus, the granulation pattern does not change as much with flux emergence, and the distribution of spicules driven by collapsing granules is similar in both bands of loop footpoints for simulation B1. In contrast, the spicules driven by collapsing granules in simulation A2 are more frequently located in the region x = [5-8] Mm. This is because in this simulation the flux emergence close to that region impacts the granulation more significantly.

The spicules driven by magnetic energy release occur more frequently in the left band of footpoints. This is true in both simulations and could be a result of the interaction between the rising magnetic flux and the ambient field.

3.3. Dynamics

In general, all the spicules studied in this paper are the result of upwardly propagating shock waves. In order to understand the dynamics of spicule evolution in more detail, and in particular, how spicules are excited by the different drivers, we use figures 6-9. We will first explain the terms shown in the figures, which then will be used to study spicule evolution and analyze how the various drivers cause spicules.

Figure 6 shows three clear examples of spicule-like jets driven by a collapsing granule (first column), by magnetic energy release in the photosphere (second column), and by

magnetic energy release in the chromosphere (third column). From the top to bottom row we show the logarithmic temperature, upflow velocity and vertical acceleration as a function of height and time. The particle trajectory (blue line in the first row of Fig. 6) is derived by calculating the vertical displacement of a particle chosen at the beginning and bottom of the spicule. We ignore the horizontal movement for this calculation. The figure shows that the particle follows the trajectory of the spicule quite well. The differences are caused by not considering horizontal displacement, approximations of the initial point of the spicule, and the numerical error of the displacement. For illustration purposes we also draw a trace of a signal propagating from the root of the spicule with the sound speed (blue).

Figures 7-9 illustrate the physics of spicule-like jets driven by a collapsing granule, magnetic energy release in the photosphere, and magnetic energy release in the chromosphere. We show as a function of time and height a range of parameters that play an important role in the momentum and energy balance of the atmosphere. From top to bottom and left to right: relative pressure perturbation P/P>-1, vertical pressure gradient perturbation $(\partial P/\partial z)/P/\partial z>-1$, gravity perturbation, i.e., the buoyancy force perturbation $g\rho/P/\partial z>-1$, vertical Lorentz force perturbation $F_{Lz}/P/\partial z>-1$, the time derivative of the gas pressure per unit of mass $(1/\rho)\partial P/\partial t$, Joule heating per unit of volume normalized with the square root of the gas pressure $\rho q_{joule}/\sqrt{P}$, heat advection term per unit of mass $-\mathbf{u}\cdot T\nabla s$, non-adiabatic heating per unit of mass (which we extract from the time derivative of the gas pressure by subtracting the adiabatic advection contribution), and the adiabatic advection term per unit of mass $(1/\rho)c_s^2\nabla\cdot(\rho\mathbf{u})$. The brackets $<\cdots>$ denote temporal averaging, $\Gamma_3-1=(\partial \ln T/\partial \ln \rho)_s=(\partial P/\partial e)_\rho$ and ρ , \mathbf{u} , e, T, s, c_s and g are the density, velocity field, specific internal energy, temperature, specific entropy, sound speed and the constant of gravity acceleration, respectively.

The pressure gradient perturbation imposes an upwards force when it is white, whereas the gravity perturbation imparts a downward force when it is white in figures 7-9. In other words, when both the pressure gradient and the gravity perturbation are white, then these forces are counteracting one another.

The middle and bottom-middle images and last column of the figures 7-9 show various terms contributing to the energy conservation equation. We can write the time derivative of pressure as:

$$\frac{\partial P}{\partial t} = -c_s^2 \nabla \cdot (\rho \mathbf{u}) + (\Gamma_3 - 1)\rho(q_{joule} + q_{rad} + q_{visc} + q_{\kappa} - \mathbf{u} \cdot T \nabla s)$$
(4)

where q_{joule} , q_{rad} , q_{visc} , q_{κ} are the specific heating terms from Joule dissipation, radiation, viscosity and thermal conduction, respectively. The Joule heating is defined as $q_{joule} = J^2/\sigma$,

where σ is the electrical conductivity. The specific heating by conduction is defined in the code as $q_{\kappa} = -\nabla(\kappa_{||}\nabla_{||}T)$, where the conduction is along the field lines (see Paper I for details). $\kappa_{||}$ is the conduction coefficient parallel to the field lines. The first term on the right hand side is the adiabatic contribution from the mass flux divergence. The second term is the non-adiabatic contribution arising from an imbalance between heating/cooling in a volume and the advection of heat into or out of the volume.

3.3.1. Spicule dynamics

All the spicules we study here are characterized by a parabolic evolution with time of the top of the spicule, *i.e.*, the transition region. This is illustrated in Fig. 6, which shows the logarithmic temperature evolution of the plasma. The vertical velocity profile in this figure shows that the plasma in the spicule first moves upwards (white), followed by downward motion (black). The shock that drives the plasma upward is seen to propagate upwards with supersonic speed. The vertical acceleration panel shows upwards acceleration just before and below the spicule (white). Once the shock reaches the transition region, the plasma in the spicule shows deceleration (black) until the end of the spicule's life. This scenario is very similar to that found in the 1D and 2D simulations of Heggland et al. (2007) and Hansteen et al. (2006), respectively.

Let us now study the momentum balance in more detail. The buoyancy force, pressure gradient force, and Lorentz force are all normalized with the temporal average of the pressure gradient, so that the figures can be compared directly. At the beginning stages of the spicule's evolution, there is typically a gas overpressure (white color, panel a) of figures 7-9). Before the spicule reaches its maximum height, this changes and becomes an underpressure (black color, panel a) of figures 7-9). While this pressure pulse reaches the transition region, we find that it originates in the lower chromosphere or photosphere depending on the driver. We will discuss the differences between each driver later. The pressure perturbation leads to an enhanced pressure gradient. The pressure gradient that originates in the driving region increases which leads to greater upflow velocities in the spicule. The gravity force increases (white), i.e., dense plasma is lifted upwards, but it is not until the perturbation reaches the transition region that the overdense plasma is sufficient to compensate for the higher pressure gradient. The overdensity remains almost until the end of the spicule's evolution. The vertical Lorentz force is negligible in the evolution of the spicule compared to the pressure gradient and buoyancy force.

Just at the top of the spicule, in the boundary between the transition region and the body of the spicule, the temporal variation of the pressure (panel e) of Figs. 7-9) is negative

(black). However, in the lower parts of the spicule, the variation of the pressure in time is positive (white). This increase in pressure follows the spicule trajectory when the spicule is increasing in length. Once the spicule reaches its maximum length, the variation of pressure in time is negative (black) and it follows the spicule trajectory back to lower heights. Joule heating (panel f) of Figs. 7-9) is not important inside the spicule, though it appears that in some cases Joule heating could play a role above the spicule. The advection term (panel g) of Figs. 7-9) is cooling (black) before, but heating after the spicule reaches its greatest length. Before the spicule reaches its maximum extent, cooling (black) by non-adiabatic advection (panel h) of Figs. 7-9) is strongest in the transition region and in a region extending 500 km downwards from the transition region. After reaching maximum extent, heating by non-adiabatic advection occurs in the same region. The advection term (panel i) of Figs. 7-9) is more important than the non-adiabatic contribution in the body of the spicule. The non-adiabatic term has the opposite sign of the adiabatic term. In other words, a positive contribution from the non-adiabatic term can balance the work done by adiabatic expansion (i.e., a negative adiabatic contribution) and/or increase the pressure.

3.3.2. The dynamics of the driving mechanism

Spicule dynamics are the same irrespective of the driving mechanism, as can be seen in the different columns of Fig. 6. However, in the convection zone, photosphere, and lower chromosphere the dynamics are different for the driving mechanisms we consider here, *i.e.*, collapsing granules, magnetic energy release in the photosphere, and magnetic energy release in the chromosphere.

Skartlien et al. (2000) have already described in detail the dynamics of collapsing granules and how these events can perturb the chromosphere. The results we find here are similar to those of Skartlien et al. (2000): We find that the photospheric perturbation associated with collapsing granules can perturb the chromosphere and produce a spicule. In short, in the convection zone the vertical mass flux divergence is compensated by horizontal mass flux convergence of fluid from neighboring granules. The collapsing granule undergoes a strong downward acceleration (see the dark feature which starts at 400 s and $z \sim 0$ Mm panel c) of figure 6). In the upper photosphere ($z \approx 200$ km), the fluid is initially (300 s) accelerated downwards, but at $t \approx 400$ s upwards, which produces a rarefaction followed by a compression and then decaying oscillatory wake. This wake becomes a shock, around $t \approx 750$ s, in the transition region ($z \approx 1800$ km) with velocities of the order of 30 km s⁻¹.

When the granule collapses ($\sim 400 \text{ s}$, $z \sim 0 \text{ Mm}$), the adiabatic pressure (panel i) of Fig. 7) changes from a negative (black) to a positive (white) contribution, and the time

derivative of the pressure (panel e) of Fig. 7) becomes positive (white). This perturbation propagates to higher and lower layers but it is largely compensated by the non-adiabatic contribution (panel h) of Fig. 7). Advective heating (panel g) of Fig. 7) dominates the non-adiabatic processes in a region from the lower chromosphere up to near the transition region ($z \approx [1-2]$ Mm).

Figure 8 and the middle column of figure 6 show an example of a spicule driven by photospheric magnetic energy release which can be seen in the panel f) of Fig. 8 during a period of time from 50 to 200 s. The energy release is slightly extended in height and time. When a spicule is driven by photospheric magnetic energy release, an upwards acceleration in the upper photosphere is produced (shown in white in the panel f) of Fig. 6 around $t \approx 350$ s and $z \sim 0$ Mm). As a result of the upward acceleration, the dynamics above the photosphere are similar to those we find for collapsing granules. However, in the photosphere and below the location of the driver, the dynamics are different. There is a small downward acceleration for a short time period (dark color around $z \approx [(-500) - 0]$ km at time $t \approx [320 - 400]$ s at panel f) of Fig. 6). An overpressure appears when the wave propagates into the chromosphere (white color in the panel a) of Fig. 8 at roughly $z \approx 1000$ km and $t \approx 550$ s), as well as an excess in pressure gradient (white color of the panel b) of Fig. 8 at a similar time and height as the overpressure). We find that an excess in density appears over a larger region in time and height, which is opposite to the change in pressure gradient and a bit higher in amplitude (but a similar order of magnitude) when the wave gets closer to the chromosphere. In addition to this, we note that there is no adiabatic (panel i) of Fig. 8) nor non-adiabatic (panel h) of Fig. 8) contribution in the convection zone related with this type of driver: the convection does not seem to notice the magnetic energy release event.

Let us now focus on chromospheric magnetic energy release (see the example shown in the last column of figure 6 and figure 9). In that example the magnetic energy release is located in a narrow range in time and space, at a height of 1 Mm above the photosphere and at $t \approx 900$ s as shown in the panel f) of figure 9. We again find that above the magnetic energy release site the dynamics are similar to what occurs for the other drivers. However, below the magnetic energy release (lower chromosphere and photosphere) the dynamics are different. The magnetic energy release produces a downward acceleration (in darkish color starting at $t \approx 900$ s and at $z \approx 1$ Mm panel i) of Fig. 6) which propagates towards the photosphere. The rarefaction and subsequent compression are nearly in phase below the magnetic energy release height (see panels g) and g) of Fig. 9 at times g00 s). An excess in pressure gradient (panel g00 f Fig. 9), balanced by an excess in density (panel g00 of Fig. 9), appears when and where the magnetic energy release takes place (around 900 g0 and at g1 Mm). These increases in density, pressure, and pressure gradient move with the spicule until it reaches its maximum extent, but also remain for a few minutes at the height

 $(z \approx 1 \text{ Mm})$ where the magnetic energy release takes place. However, these increases do not extend down to below the photosphere.

For both types of spicule driven by magnetic energy release, the adiabatic pressure increases just above the location of the driver and the time derivative of pressure becomes positive and propagates to higher and lower layers ($z \approx 0$ km and $t \approx 320$ s for the photospheric magnetic energy release shown in Fig. 8 and $z \approx 1$ Mm and $t \approx 900$ s for the chromospheric magnetic energy release shown in Fig. 9). This is counteracted by the non-adiabatic contribution. However, this changes rapidly in higher layers, close to the transition region, where we find a growing adiabatic contribution. Below roughly $z \approx 1.5$ Mm the adiabatic contribution is compensated by non-adiabatic contribution. At greater heights the advective heating dominates the non-adiabatic contribution, *i.e.* in the region confined between the lower chromosphere to near the transition region (see panel g) of Fig. 8 and 9).

4. Discussion and conclusions

Our 3D simulations naturally produce structures that resemble observed type I spicules. These models represent a significant improvement over the 1D and 2D simulations that have been used to study these kinds of spicules in the recent past (Heggland et al. 2007; Hansteen et al. 2006), since they are the most realistic 3D radiative MHD simulations to date. Similar to the 2D simulations, the current simulations include non-grey and non-LTE radiative transfer with scattering, thermal conduction along the field lines, and a convectively unstable convection zone. The current simulations also include a full 3D approach, a corona that is maintained self-consistently with temperatures greater than 5 10⁵ K, and flux emergence.

In total we found 168 spicules of which 150 follow a clear parabolic trajectory in which the transition region is first pushed upwards by denser chromospheric plasma, and then retreats back during the second half of the spicule's life. In analyzing these spicules we follow the approach taken by Hansteen et al. (2006) and De Pontieu et al. (2007a): we determine the deceleration, maximum velocity, duration and maximum height from parabolic fits. We find that the ranges of values for deceleration and maximum velocity are similar to those found for spicular jets in previous simulations, and for spicules, mottles and fibrils found in observations.

The ranges of values for duration and maximum height are smaller than those found in observations and previous simulations. All the jets we find here have durations of order 2-3 minutes, whereas observations show a wider variety of durations, from 2 to 8 minutes.

In addition, we find rather short jets in the 3D simulations, with lengths typically less than 2000 km. It is likely that a combination of limitations of the numerical simulations is the cause for these discrepancies. For example, the duration and shorter lengths of the simulated jets are actually quite similar to those found in observations of dynamic fibrils that occur in a dense plage region where the magnetic field is more vertical. It is thus likely that the limited range of magnetic field configurations in our simulations as compared to the variety of magnetic environments that the real Sun presents plays a role in this discrepancy.

Additionally, our selection criterion imposes a minimum height of 2000 km on the spicules. This provides a bias towards vertical features, since it potentially removes candidate spicules that are heavily inclined and that form along the magnetic canopy. These inclined spicules may not cause much of a transition region height excursion, but may well be an important fraction of what we observe on the disk on the Sun as indicated by the heavily inclined dynamic fibrils that dominate the less dense plage region discussed by (De Pontieu et al. 2007a). These inclined spicules are also seen to form regularly in previous 2D simulations (Hansteen et al. 2006). Another bias that leads to vertically oriented spicules in this paper is that the field lines that extend into the corona, *i.e.* the field lines on which spicules occur, are essentially vertical in the magnetic field topology modeled in both models. Field lines that close lower in the chromosphere may hinder the formation of spicules through the processes of wave mode conversion and reflection as described by *e.g.* Rosenthal et al. (2002) and Bogdan et al. (2003).

One of the mechanisms that is thought to drive a significant fraction of spicule-like jets in the atmosphere (De Pontieu et al. 2004), i.e., leakage of p-mode oscillations, likely play a significant role in the group "other mechanisms", which constitutes 26% of our spicules in both simulations. For half of these spicules, we find a correspondence between the timing of p-modes oscillations in the photosphere and the initiation of the chromospheric waves. The p-modes in the simulations are stochastically excited by the convective motions but the lower cavity boundary is given by the simulation box rather than by refraction in the deep convection zone. The resulting modes are therefore rather few but the total power is similar to the solar case. At $z=200~\mathrm{km}$ we have an rms velocity amplitude of 260 m s⁻¹ in the oscillation component (horizontal phase speed larger than 6 km s⁻¹) below a frequency of 4.5 mHz. This value is of the same order as the observed rms velocity amplitude of 202 m s⁻¹ in MDI high-resolution data (Straus et al. 1999) that is filtered in the same way (Straus, T.: 2009, personal communication). The smaller number of modes present in the simulations compared with the Sun may, however, lead to fewer occurrences of large amplitude, constructive interference events. In addition, propagation of p-mode oscillations into the chromosphere (and subsequent spicule formation) are facilitated by the presence of inclined magnetic field lines, which are rare in the magnetic field configurations in our models. These two factors may help explain the relatively low occurrence rate of p-mode driven spicules in the simulations we analyze here.

Another factor that could reduce the strength of the upwardly propagating shocks in our simulations compared to the Sun is the treatment of hydrogen ionization. In our simulation it is implicitly assumed that hydrogen ionizes or recombines immediately as a result of changes in the temperature and density. Carlsson & Stein (2002); Leenaarts et al. (2007b) and Leenaarts et al. (2007a) have shown that this is not the case and that a proper treatment of hydrogen ionization can have a significant impact on shock characteristics in the upper chromosphere. This is because the energy going into ionization in the current simulations would be available for heating the plasma and thus strengthening the shocks.

Finally, it is likely that the low numerical resolution in the chromosphere and transition region in both the horizontal and vertical direction play an important role in the discrepancy between jets in the simulations and observed jets. The resulting sizable numerical diffusion can significantly reduce the strengths of shocks, which can lead to jets of reduced amplitude (and thus reduced duration, since we impose a minimum height of 2000 km). We expect that increasing the number of grid points (and thus decreasing the viscosity and diffusion) of the computational domain can lead to significant differences in the properties of the spicules, especially with respect to the height and duration.

Despite all of these differences, we find many similarities between observations and our simulations with respect to the correlations between various parameters. Hansteen et al. (2006) and De Pontieu et al. (2007a) find a host of correlations between the deceleration, maximum velocity, length and duration of dynamic fibrils. The spicule-like features in our simulations reproduce these correlations remarkably well. This is because the underlying cause for these correlations is shock-wave physics, as discussed at length by Heggland et al. (2007). Our simulations here show in detail how the parabolic trajectory of the spicules is caused by upper chromospheric flows driven by a shock wave propagating upward after being generated below the spicule. Detailed analysis of the momentum and energy balance in our 3D simulations shows that the pressure gradient resulting from the shock wave passage counteracts the gravitational force. This naturally leads to a trajectory that is not a purely ballistic trajectory: the shock wave and its associated pressure gradient provide an ongoing force against gravity. As a result, we find decelerations that are substantially different from solar gravity (similar to what was found in previous simulations and the observations). The spicule trajectory is a natural result of the motion induced by the upflows and downflows in the wake of the shock wave that ultimately propagates into the corona. In addition, the non-adiabatic contribution to the energy balance counteracts the adiabatic contribution during the early evolution of the spicule.

The type I spicules in our simulations (and previous simulations) are formed by upwardly propagating chromospheric waves that form into shocks. In our simulations, we manage to identify several different driving mechanisms: collapsing granules, magnetic energy release in the photosphere and magnetic energy release in the low chromosphere. We also identified other candidates, such as p-modes, convective buffeting by breaking granules, and magnetic field topology changes resulting from flux emergence. This list is not exhaustive, since our simulations clearly show that any mechanism that produces a chromospheric wave or perturbation that develops into a shock and propagates along a flux concentration can drive type I spicules. It is thus likely that there are more/other physical processes that can produce the waves that drive type I spicules. Given the complexities of the 3D simulations, it is generally quite difficult to pinpoint the driving mechanism for the waves that drive each spicule. We find that as long as a perturbing event creates a perturbation close to a flux concentration that reaches into the chromosphere and corona, a spicule can develop. The properties of the spicules do not seem to change much for the various driving mechanisms that we identified, except perhaps when magnetic energy is released in the chromosphere. In that case, there seems to be a slightly different relation between deceleration and maximum velocity, which is concentrated in the upper part of the distribution of points (see Fig. 1).

The magnetic energy release events described here involve regions where the current is highly localized and Joule dissipation is locally significantly enhanced, with a subsequent perturbation propagating away from the dissipation site. Some of these events might be related to magnetic field line reconnection, although in most cases reconnection of field lines is difficult to identify. Our simulations suggest (see also Heggland et al. 2009) that, in principle, sudden energy release (e.g., from reconnection) in the low atmosphere can lead to both type I and type II jets. Our simulations contain a few events that are more violent with shorter lifetimes and higher velocities that are similar to type II spicules. These jets will be described in future work. It is clear however that the underlying formation mechanism and/or magnetic configuration is different between these two types of events.

The importance of the magnetic field configuration in producing type I spicules is significant. While our simulations do not cover a wide range of field configurations (unipolar plage, mixed polarity quiet Sun, open field in coronal holes), we already notice from our two different simulations that the number of spicules increases with the strength of the ambient field and that they become shorter, which is similar to what is observed on the Sun. The most important impact of field configuration entry into the corona lies in the different driving mechanisms that are expected to dominate in different field topologies. For example, our simulations involve emergence of an intense magnetic flux tube. It is thus not surprising that about half of the events we find are driven by magnetic energy release, most likely related to the emergence of new field into a pre-existing ambient field. Such conditions are not typical

for plage regions or most quiet Sun regions, so that we should be careful in extrapolating the importance of the different mechanisms to the real Sun. One of the two driving mechanisms that we expect to occur everywhere on the Sun, *i.e.*, convective buffeting of flux concentrations, is shown to play an important role in producing spicules in our simulations, and can be expected to play a similar role on the Sun.

5. Acknowledgments

This research has been supported by a Marie Curie Early Stage Research Training Fellowship of the European Community's Sixth Framework Programme under contract number MEST-CT-2005-020395: The USO-SP International School for Solar Physics. Financial support by the European Commission through the SOLAIRE Network (MTRN-CT-2006-035484) is gratefully acknowledged. The 3D simulations have been run with the Njord and Stallo cluster from the Notur project and the Columbia cluster of NASA's High-End Computing Program. We thankfully acknowledge the computer and supercomputer resources by the Research Council of Norway through grant 170935/V30 and through grants of computing time from the Programme for Supercomputing. BDP was supported by NASA grants NNM07AA01C (HINODE), NNG06GG79G and NNX08AH45G. To analyze the data we have used IDL and Vapor (http://www.vapor.ucar.edu).

REFERENCES

Beckers J. M., 1968, Sol. Phys., 3, 367

Bogdan T. J., Carlsson M., Hansteen V. H., et al., 2003, ApJ, 599, 626

Carlsson M., Stein R. F., 1992, ApJ, 397, L59

Carlsson M., Stein R. F., 1995, ApJ, 440, L29

Carlsson M., Stein R. F., 1997, ApJ, 481, 500

Carlsson M., Stein R. F., 2002, ApJ, 572, 626

Cheung M. C. M., Moreno-Insertis F., Schüssler M., 2006, A&A, 451, 303

De Pontieu B., Erdélyi R., de Wijn A. G., 2003, ApJ, 595, L63

De Pontieu B., Erdélyi R., James S. P., 2004, Nature, 430, 536

- De Pontieu B., Hansteen V. H., Rouppe van der Voort L., van Noort M., Carlsson M., 2007a, ApJ, 655, 624
- De Pontieu B., McIntosh S. W., Hansteen V., Carlsson M. P., 2007b, AGU Fall Meeting Abstracts, C8
- Dorch S. B. F., Nordlund A., 1998, A&A, 338, 329
- Fan Y., Zweibel E. G., Linton M. G., Fischer G. H., 1998, ApJ, 505, L59
- Gudiksen B. V., Nordlund Å., 2004, en IAU Symposium, Vol. 219, Dupree A. K., Benz A. O. (eds.), Stars as Suns: Activity, Evolution and Planets, p. 488
- Hansteen V. H., De Pontieu B., Rouppe van der Voort L., van Noort M., Carlsson M., 2006, Apj, 647, L73
- Heggland L., De Pontieu B., Hansteen V. H., 2007, ApJ, 666, 1277
- Heggland L., De Pontieu B., Hansteen V. H., 2009, ArXiv e-prints
- Hyman J., Vichnevtsky R., Stepleman R., 1979, Adv. in Comp. Meth, PDE's-III, 313
- Judge P. G., Meisner R. W., 1994, The 'HAO spectral diagnostics package' (HAOS-Diaper), en ESA Special Publication, Vol. 373, Hunt J. J. (ed.), Solar Dynamic Phenomena and Solar Wind Consequences, the Third SOHO Workshop, p. 67
- Leenaarts J., Carlsson M., Hansteen V., Rutten R. J., 2007a, A&A, 473, 625
- Leenaarts J., Wedemeyer-Böhm S., Carlsson M., Hansteen V. H., 2007b, en Coimbra Solar Physics Meeting ion the Physics of Chromospheric Plasmas, ASP Conference Series, Vol. in this volume, This volume
- Linton M. G., Longcope D. W., Fisher G. H., 1996, ApJ, 469, 954
- Mackay D. H., Galsgaard K., 2001, Sol. Phys., 198, 289
- Martínez-Sykora J., Hansteen V., Carlsson M., 2008, ApJ, 679, 871
- Martínez-Sykora J., Hansteen V., Carlsson M., 2009, ApJ, submitted
- Nordlund Å., 1982, Aap, 107, 1
- Rosenthal C. S., Bogdan T. J., Carlsson M., et al., 2002, ApJ, 564, 508

Rouppe van der Voort L. H. M., De Pontieu B., Hansteen V. H., Carlsson M., van Noort M., 2007, ApJ, 660, L169

Scharmer G. B., Narayan G., Hillberg T., et al., 2008, ApJ, 689, L69

Skartlien R., 2000, ApJ, 536, 465

Skartlien R., Stein R. F., Nordlund Å., 2000, ApJ, 541, 468

Straus T., Severino G., Deubner F.-L., et al., 1999, ApJ, 516, 939

Tsuneta S., Ichimoto K., Katsukawa Y., et al., 2008, Sol. Phys., 249, 167

This preprint was prepared with the AAS LATEX macros v5.2.

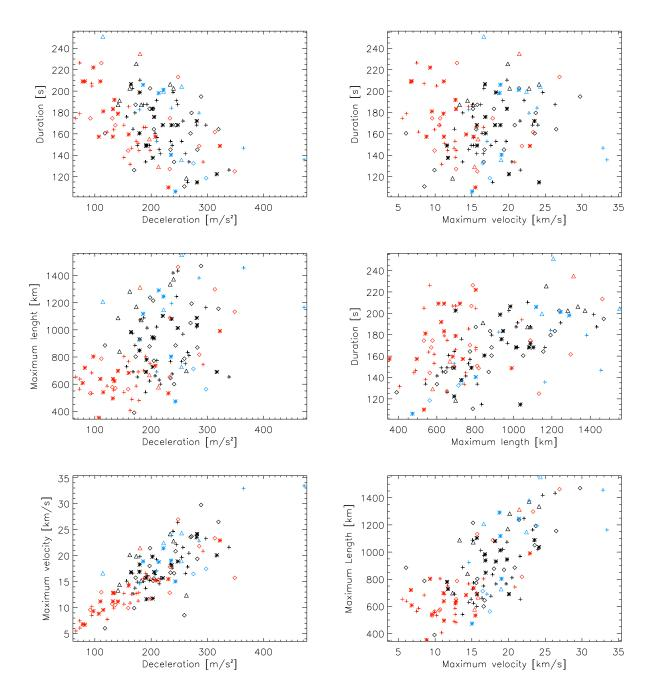


Fig. 1.— Scatterplots of parabolic parameters for all 150 type I spicules measured in the simulations. Duration vs. deceleration of the spicules, maximum length vs. deceleration, maximum velocity vs. deceleration, duration vs. maximum velocity, duration vs. maximum length and length vs. maximum velocity are illustrated from top to bottom and left to right. The spicules from simulation A2 during the temporal range [300-3200] s are shown in black and the spicules during the temporal range [3800-5100] s in blue. Spicules from simulation B1 are shown in red. The deduced driving mechanism is shown with symbols: collapsing granules (plus sign), photospheric magnetic energy release (rhombus), chromospheric magnetic energy release (triangle) and other or unidentified mechanisms (asterisk).

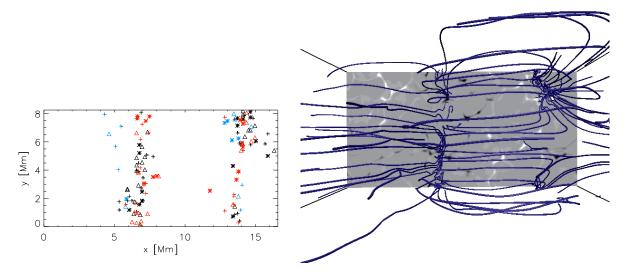


Fig. 2.— Map showing the (x,y) locations of the spicules (left panel). The spicules from simulation A2 during the temporal range [300-3200] s are shown in black and the spicules during the temporal range [3800-5100] s in blue. Spicules from simulation B1 are shown in red. The driving mechanism is shown with symbols: collapsing granules (plus symbol), magnetic energy release (triangle) and other mechanisms (asterisk). The right panel shows a view from above of the computational domain of the simulation A2 showing field lines traced from the corona (blue lines) and the vertical magnetic field strength in the photosphere (grey-scale).

Table 1. Summary of the parameters which describe the two simulations. From left to right, the assigned name, the twist of the tube, the magnetic field strength of the tube, the size of the computational box, the duration of the simulations, the radius of the tube and the ambient field measured at the photosphere.

Name	Twist λ	B ₀ [G]	Size $[Mm^3]$	Time [s]	Radius [Mm]	Ambient field [G]
A2	0.6	4484	$16 \times 8 \times 16$	5700	0.5	16
B1	0	1121	$16 \times 8 \times 16$	4400	1.5	160

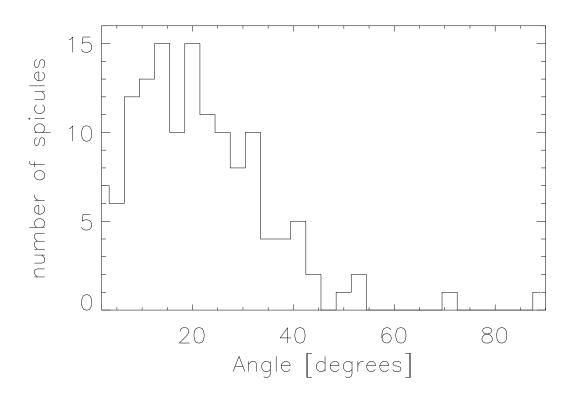


Fig. 3.— Histogram of the angle between the vertical axis and the direction of the field lines which go through the spicules. Most of the spicule angles are between 10^{o} and 30^{o} .

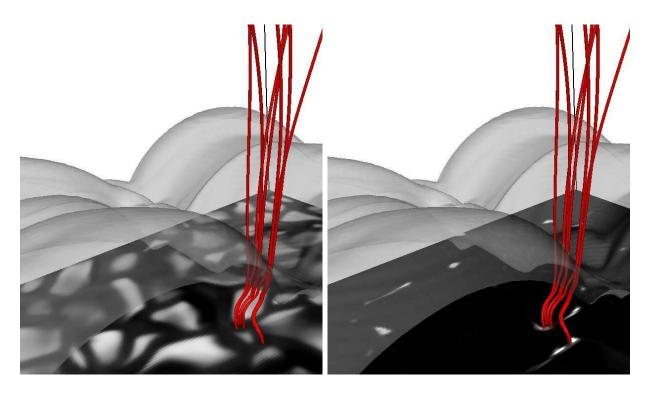


Fig. 4.— Magnetic field geometry and connection to the photosphere of a spicule driven by a collapsing granule. Temperature in the photosphere is shown in a flat surface in grey color scale in the left 3D image. In the right 3D image, the absolute magnetic field strength in the photosphere is shown with a flat surface in grey color scale with a range of [0-12] G. The (semitransparent) grey isosurface is the transition region at $T=10^5$ K. The red lines come from a spicule which is formed by a collapsing granule which is surrounded by the field lines. The spicule forms along the strongest concentration of flux and where the field lines go into the corona.

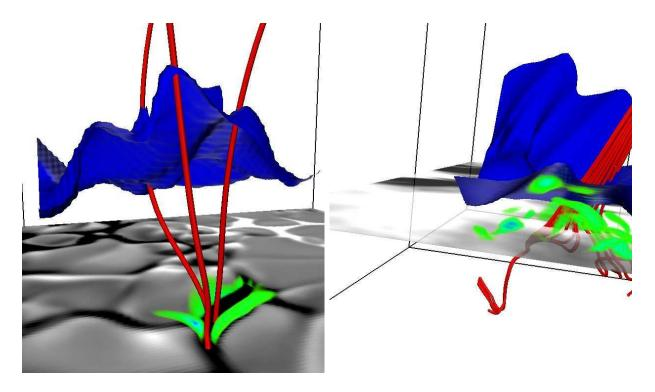


Fig. 5.— Magnetic field geometry and connection to the photosphere of three different spicules driven by magnetic energy release in the photosphere (left panel) and magnetic field geometry and connection to the chromosphere of a spicule driven by magnetic energy release in the chromosphere (right panel). Vertical magnetic field strength is shown in grey color scale; in the left 3D image at the photospheric level with a range of ± 12 G, and in the right 3D image at the chromosphere level (z=1 Mm) with a range of ± 5.6 G. The transition region ($T=10^5$ K) is shown with the blue isosurface. The current over the square root of the gas pressure (R_d , see Eq. 3) shows regions where magnetic energy dissipation is high (green color). The three field lines shown in red in the left image end up in three different spicules but trace back to the same driver in the photosphere, a magnetic energy release event. The lines are concentrated in the intergranular lane in association with a strong magnetic flux concentration. The right image shows an example of a spicule driven by magnetic energy release in the chromosphere. Here the field lines are concentrated in a flux concentration at chromospheric heights, but spread out significantly at lower heights.

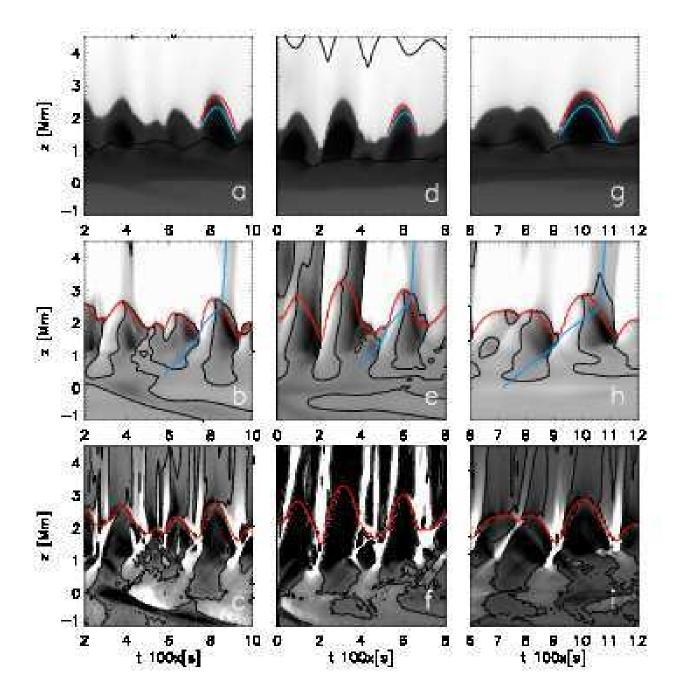


Fig. 6.— Logarithmic temperature, vertical velocity and vertical acceleration as a function time and of height is shown from top to bottom row respectively. The black contour in the first row is $\beta = 1$, in the other images it shows where the plotted parameter is zero. In the first row, the parabolic fit is plotted with a red line, and the particle trajectory with a blue line. The second and third row show the transition region ($T = 10^5$ K) as a red line. In the middle row, the blue line shows the path a perturbation propagating at the speed of sound would take. The first column shows a spicule that starts at 750 s and that is driven by a collapsing granule at time 400 s. The second column shows a spicule that starts at 550 s and that is produced by a photospheric magnetic energy release event at time 400 s. The

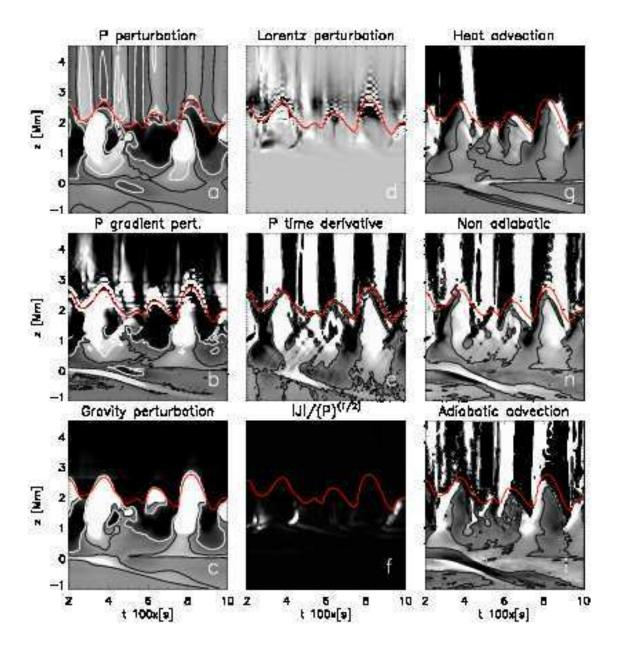


Fig. 7.— The following parameters are shown from top to bottom and from left to right as functions of height and time: Pressure perturbation (white is overpressure), pressure gradient perturbation (white is upwards force), gravity perturbation (white is downwards force), vertical Lorentz force perturbation (white is upwards force), time derivative of pressure (white is increase in pressure), R_d term, see Eq. 3 (white is large magnetic discontinuity), heat advection term (white is large contribution), non-adiabatic contribution (white is heating) and adiabatic contribution (white is heating). The black contour shows when the parameter is zero. The white contours show perturbation of $\pm 10\%$. The red line is the transition region $(T = 10^5 \text{ K})$. The example shown here is the same spicule that is shown in the first column of Fig. 6, which is driven by a collapsing granule. The checkerboard pattern observed mostly in the transition region in some panels (e.g., the Lorentz perturbation), is caused by the numerical noise and spatial and temporal resolution in the transition region and corona.

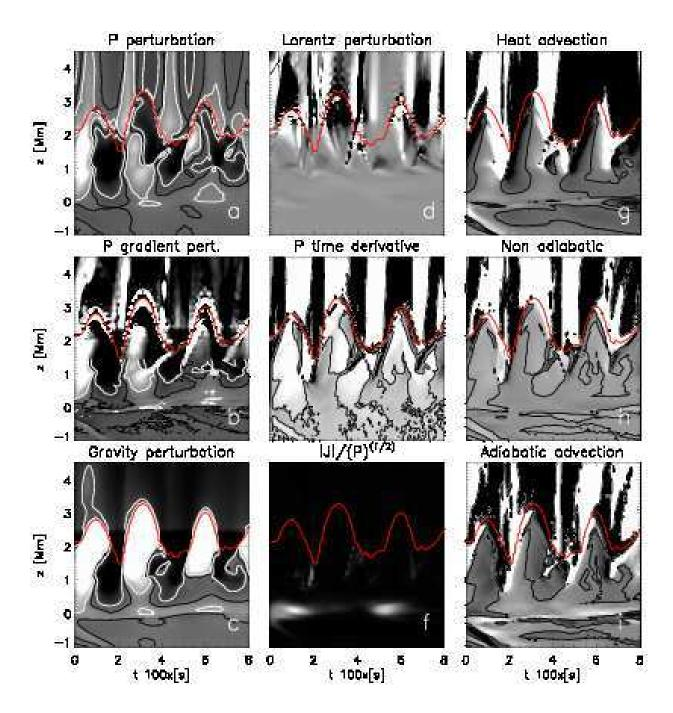


Fig. 8.— Same terms, parameters and color scheme as described in figure 7 in the same order. The example shown here is the same spicule that is shown in the second column of figure 6, which is driven by photospheric magnetic energy release.

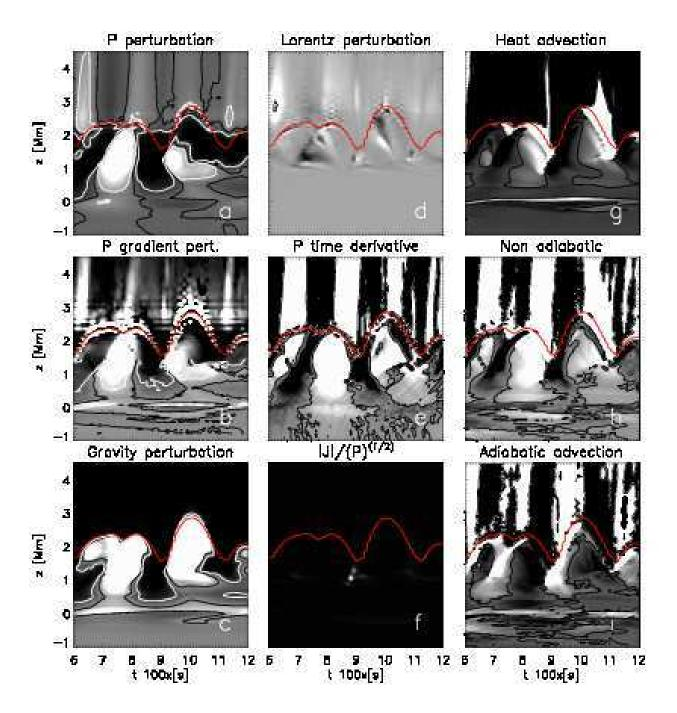


Fig. 9.— Same terms, parameters and color scheme as described in figure 7 in the same order. That correspond a spicule driven by a chromospheric magnetic energy release shown in the third column of figure 6.